Unified framework for laser-induced transient bubble dynamics within microchannels

Nagalingam, Nagaraj; Korede, Vikram; Irimia, Daniel; Westerweel, Jerry; Padding, Johan T.; Hartkamp, Remco; Eral, Hüseyin Burak

DOI
10.1038/s41598-024-68971-x

Publication date
2024

Document Version
Final published version

Published in
Scientific Reports

Citation (APA)
Nagalingam, N., Korede, V., Irimia, D., Westerweel, J., Padding, J. T., Hartkamp, R., & Eral, H. B. (2024). Unified framework for laser-induced transient bubble dynamics within microchannels. *Scientific Reports*, *14*(1), Article 18763. https://doi.org/10.1038/s41598-024-68971-x

scientific reports

Check for updates

OPEN

Unified framework for laser-induced transient bubble dynamics within microchannels

Nagaraj Nagalingam, Vikram Korede, Daniel Irimia, Jerry Westerweel, Johan T. Padding, Remco Hartkamp & Hüseyin Burak Eral✉

Oscillatory flow in confined spaces is central to understanding physiological flows and rational design of synthetic periodic-actuation based micromachines. Using theory and experiments on oscillating flows generated through a laser-induced cavitation bubble, we associate the dynamic bubble size (fluid velocity) and bubble lifetime to the laser energy supplied—a control parameter in experiments. Employing different channel cross-section shapes, sizes and lengths, we demonstrate the characteristic scales for velocity, time and energy to depend solely on the channel geometry. Contrary to the generally assumed absence of instability in low Reynolds number flows (< 1000), we report a momentary flow distortion that originates due to the boundary layer separation near channel walls during flow deceleration. The emergence of distorted laminar states is characterized using two stages. First the conditions for the onset of instabilities is analyzed using the Reynolds number and Womersley number for oscillating flows. Second the growth and the ability of an instability to prevail is analyzed using the convective time scale of the flow. Our findings inform rational design of microsystems leveraging pulsatile flows via cavitation-powered microactuation.

Micromachines with few mechanical components have revolutionized the areas of microelectromechanical systems (MEMS)[1–3]. The potential of bubble-powered micromachines was first realized in ink-jet printing[4], later also finding other applications that require precise flow control and rapid actuation[5–7]. Oscillatory flows are not limited to synthetic devices, but also invariably exist in nature, e.g., in cardiovascular and respiratory flows[8]. Yet characterization and optimization of pulsated oscillatory flow is underexplored compared to steady flows[2]. Therefore, a unified understanding will inform both synthetic and physiological systems, encompassing particle manipulation[9,10], rheology[11,12], emulsification[13], cell lysis[14,15], prilling[16], needleless injection[17,18] and gas embolotherapy[19].

Laser-induced cavitation allows localization of high temperature and large flow velocities due to the growth and collapse of short-lived vapor bubbles. Thus, laser light can be implemented to induce flow in processes with only need for optical access[20]. For confined geometries, the arrested directions of flow and increase in bubble lifetime due to strong confinement-induced momentum dissipation allows for a simplified theoretical and experimental approach[21,22]. Yuan et al.[23] laid the theoretical foundation for the dynamics of a vapor bubble in a narrow channel with a circular cross-section. They reported the internal vapor pressure of the bubble to be insignificant after the initial 10% of the bubble's lifetime. Thus, the dynamics of the bubble is largely governed by the wall resistance of the microchannel, ambient pressure, and inertia of the liquid shortly after bubble formation. Using experiments and a numerical model, Sun[22] showed the role of absorbed laser energy in bubble evolution within circular microchannels with internal diameters of 25 and 50 μm.

The key to rational control of thermocavitation driven flows hinges on understanding the dynamics of the transient bubble, the bubble lifetime, and its dependence on the laser energy supplied. The findings could potentially be applied to any microsystem that employs a periodic actuation source to transfer momentum to the fluid much faster than the timescale of flow oscillation. Given application-specific requirements, e.g., flow rates, droplet production rate and mixing[24], valve actuation time[25], etc., there is a need for a unified framework with which one could a priori design the channel geometry (cross-section shape, size and length), provided that the fluid properties such as viscosity, density and light absorbance are known. Beyond the design of *lab-on-a-chip* devices, characterizing the flow and instabilities will help in the study and engineering of physiological systems, such as flows in arteries and bronchioles, by additionally incorporating the effects of channel wall compliance[26].

Process and Energy Department, Delft University of Technology, Leeghwaterstraat 39, 2628 CB Delft, Netherlands. ✉email: h.b.eral@tudelft.nl

Cross-section	Hydraulic diameter (µm)	Inner diameter (µm)	Wall thickness (µm)
Circular	100	100	35
Circular	200	200	65
Circular	300	300	50
Square	100	100	50
Square	200	200	100
Square	300	300	150
Rectangle	66.7	50 × 100	50
Rectangle	126	80 × 300	56

Table 1. Microchannel specifications used in this work. Material: borosilicate, tolerance +/−10%, manufacturer: CM Scientific.

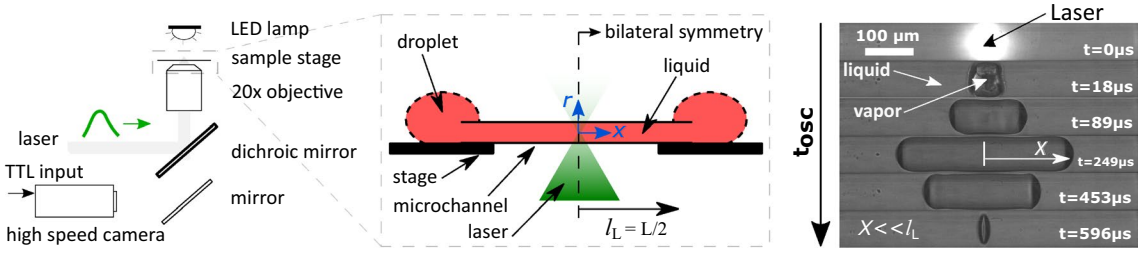

Figure 1. A sketch of the experimental setup with representative images of bubble dynamics from inception to collapse—one oscillation cycle. X represents the bubble size and t_{osc} is the bubble lifetime.

Furthermore, the fundamental understanding developed can be utilized in laser-induced crystallization via thermocavitation[27–29], as the bubble dynamics will dictate hydrodynamic flows around nucleated crystals.

In this paper, combining high-speed microscopy and an analytical approach, we demonstrate a universal dependence of the magnitude and duration of the induced flow on the laser energy supplied in microchannels with circular, square, and rectangular cross-sections. Prior works discussed undistorted laminar flows[22,30–32], which is a convenient assumption for low Reynolds numbers ($Re < 1000$)[33]. Nevertheless, we observe the occurrence of a transient flow instability even at $Re < 1000$, and delineate it by characterizing two dimensionless numbers: (i) the Reynolds number (Re), contingent on the peak mean flow velocity and channel hydraulic diameter, and (ii) the Womersley number (Wo), contingent on the bubble lifetime and channel hydraulic diameter. This momentary instability emerges due to the oscillatory nature of the flow[34,35], and results in momentary unsteady velocity profiles due to the disruption of the momentum boundary layer near the channel walls[36].

This paper first details the experiments for quantifying the dynamic bubble size and lifetime as the function of its maximum bubble size. Then the associated theoretical framework is presented to explain underlying physics. Following which, a general empirical correlation between maximum bubble size and laser energy supplied, and the minimum threshold laser energy for bubble formation is discussed. Finally, using the established theoretical framework and experiments, we characterize the flow transition limits and nature of the distorted laminar flow.

Methods

Laser setup

Frequency-doubled Nd:YAG pulsed laser with 532 nm wavelength, 4 mm beam diameter and 4 ns pulse duration. A 20× objective (numerical aperture = 0.5) is used to focus the laser within the microchannel and simultaneously used for imaging[37]. The images are recorded at 112,500 frames per second using a high-speed camera.

Working fluid

An aqueous solution of red dye (RD81, Sigma-Aldrich) with 0.5 wt% is used to have higher absorbance to light at 532 nm. The absorption coefficient (α) was measured to be 173 cm^{-1} using a spectrometer (DR6000, Hach). The liquid was not pre-treated for dissolved gases.

Channel geometry

The hydraulic diameter (d_h) of the channels range from 66.7 µm to 300 µm, with the maximum bubble half-size, $X_{max} \in [d_h/2, 2\,d_h]$ (see Fig. 1). Two different capillary lengths, $L = 25$ and 50 mm, were used for all cases with the laser always focused at the geometric center. The channel specifications used in this work are summarized in Table 1.

Results and discussion

Dynamic bubble size

Since the midpoint of the capillary and the bubble coincides, in our theoretical model we analyze only half the geometric domain owing to the bilateral symmetry, see Fig. 1. Thus, the length of the liquid column under analysis (l_L) is half the total length of the channel used, and the half-size of the bubble (X) is determined by the position of the vapor-liquid interface from the center as illustrated in Fig. 1. In the post-processing of the images the parameter X was estimated by dividing the bubble volume with the area of the channel cross-section (see Supplementary Section 1). This approach of determining X ruled out the effects of bubble end curvatures, furthermore allowing us to estimate the liquid velocities as a function of rate of volume displaced. The liquid droplets at either end of the channel act as reservoirs, thus compensating for the liquid displaced by the vapor bubble. In addition, these droplets also ensure that the evaporation of the liquid to the ambient surrounding doesn't deplete the liquid within the channel.

After attaining the capillary diameter (d_h), the vapor bubble elongates along the axial (along x) direction with the cross-section as that of the channel. Thus, for an elongated bubble, when $X \ll l_L$, the equation of motion of the liquid column within the channel is[22]

$$l_L \rho_L \frac{d^2X}{dt^2} = p_V(t) - p_\infty - \mathscr{R}\,\frac{dX}{dt}, \tag{1}$$

where ρ_L is the liquid density, $p_V(t)$ is the pressure inside bubble, p_∞ is the ambient pressure and $\mathscr{R}$ the hydraulic resistance of the channel. Due to strong confinement in two directions, the resulting flow is quasi-1D along the longitudinal axis x, which justifies the use of a one-dimensional model. The expressions of the steady state hydraulic resistance derived using laminar flow theory for different cross-sections are[38]: $32\mu_L l_L/a^2$ (circle); $28.4\mu_L l_L/a^2$ (square) and $\approx 12\mu_L l_L/[(1-0.63b/a)b^2]$ (rectangle), where μ_L is the dynamic viscosity of the liquid and a, b are the cross-section's edge lengths with $b < a$. For circular and square cross-sections $d_h = a$, and for a rectangular cross-section $d_h = 2ab/(a+b)$. By non-dimensionalizing Eq. 1, we obtain the characteristic velocity (υ) and timescale (τ) for the channel geometry as $\upsilon = (p_\infty - p_V(t))/\mathscr{R}$ and $\tau = (l_L\rho_L)/\mathscr{R}$, respectively.

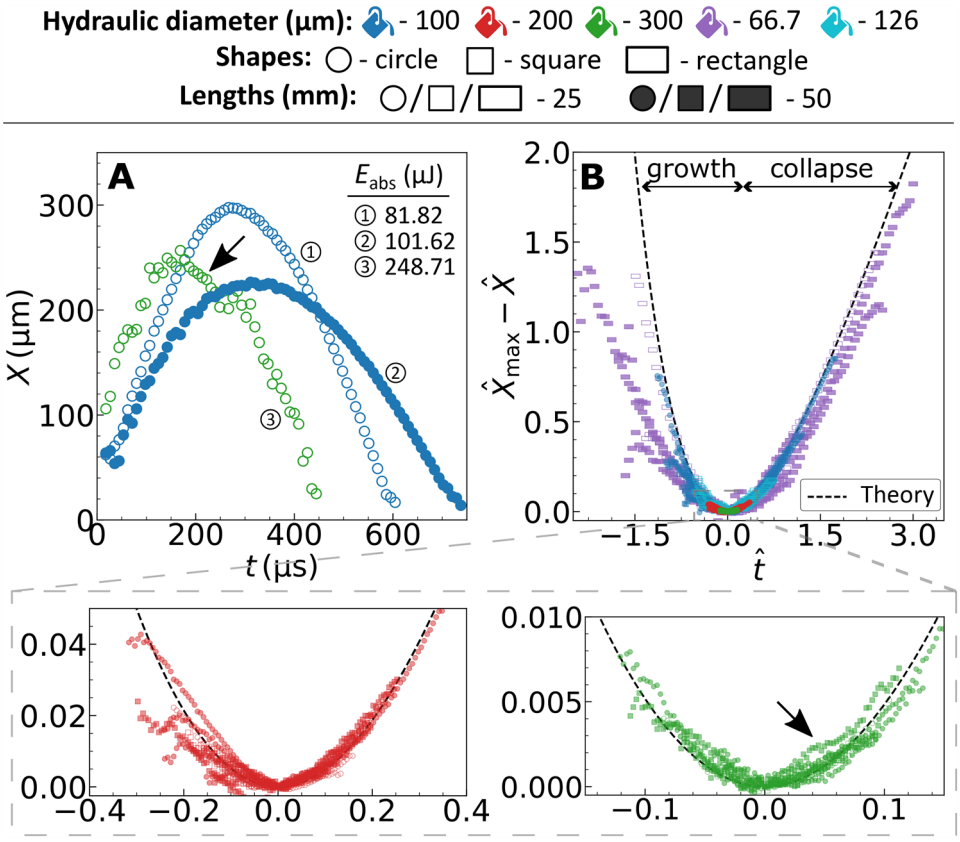

Figure 2. (**A**) Representative bubble dynamics for different channel geometries. (**B**) Universal motion of bubbles within channels with different size, shape and length. The dashed line represents the developed theory, Eq. (2). The marker colors represent the hydraulic diameters (d_h), the shapes represent the cross-section and the facecolor represent the lengths (L). The graphical marker symbols and colors established here are followed throughout this article. The black arrow represents the region of deviation(s) from the expected dynamics.

Since $p_V(t)$ is reported to be significant only during the first $\approx$ 10% of the bubble's lifetime[23], we simplify the problem by dropping this term ($p_V(t) = 0$). Thus, the liquid initially gains momentum from the impulse offered by the vapor pressure. Subsequently, the bubble continues to grow due to the liquid's inertia, even though the pressure inside the bubble is much less than the ambient pressure[22]. At the end of the growth phase, the liquid momentum is fully dissipated by the resistance of the channel walls, following which the ambient pressure collapses the bubble. We describe the bubble growth and collapse by solving the ordinary differential equation (ODE) from Eq. (1) and derive the following dimensionless equation for the dynamic bubble size:

$$\widehat{X}_{\max} - \widehat{X} = \widehat{t} + \exp(-\widehat{t}) - 1, \tag{2}$$

where $\widehat{X} = X/(\upsilon\tau)$ and $\widehat{t} = (t - t_0)/\tau$ are the dimensionless bubble size and time, respectively. The ODE is solved using the boundary condition $X = X_{\max}$ at $t = t_0$, where $X_{\max}$ is the maximum bubble size. Fig. 2A shows the representative bubble dynamics from experiments for different channel cross-sections and lengths. The bubble's maximum size, lifetime and the growth/collapse velocities vary significantly for different microchannel geometries. Figure 2B shows the experiments to follow the derived general expression for dynamic bubble size when non-dimensionalized using the characteristic scales (see Supplementary Section 1 for unscaled results).

In most cases, we see a deviation in the bubble size from theory in the first 10% of the bubble's lifetime, as expected. This can be attributed to the significant vapor pressure inside the bubble due to instantaneous phase change during formation ($\sim$ 100 bar) which then decreases abruptly due to rapid change in the bubble volume[22]. Following the phase change, in the time range of $O(\mu s)$ the vapor pressure is reported to be still very high $\sim$ 8 bar corresponding to a saturation temperature of $\sim$ 170 °C[22]. After which the change in pressure and therefore the corresponding saturation temperature is rapid, 0.15 bar/μs or 2 °C/μs approximately. Moreover, the force exerted by the channel wall during the radial (r, see Fig. 1) growth of the bubble appearing during this first 10% of the bubble's lifetime will also influence its dynamics[19]. Thus a more sophisticated theoretical model incorporating the rapid change in pressure/temperature, change in the bubble geometry from spherical to elongated, and wall forces in radial direction is necessary to accurately match the observed bubble dynamics in experiments. We therefore will overlook the accuracy within this time regime as its effect over the calculation of the characteristic parameters such as bubble lifetime, Womersley and Reynolds numbers are not large enough, discussed in detail in the following (sub)sections.

In Fig. 2A, for $d_h = 300\,\mu m$, we see a rapid acceleration during the start of the bubble collapse (pointed using a black arrow). Similarly, in Fig. 2B, we also see a deviation from theory during the start of bubble collapse becoming more significant with increasing hydraulic diameter ($d_h \geq 200\,\mu m$). We attribute these to instabilities, discussed in detail under the section "Emergence of instabilities" later in this article.

Bubble lifetime

While the dynamic size of the vapor bubble quantifies the liquid velocity or flow rate, the lifetime of the oscillating bubble governs the oscillatory time period of flow. In this work, we focus on the primary expansion and collapse of the bubble and ignore the bubble rebound caused by high pressures and temperatures[39]. Thus, the lifetime of the bubble is the time taken for one oscillation, t_{osc}. In Eq. (2), by substituting $\widehat{X} = 0$, we obtain the bubble's time of formation and collapse. The analytical prediction of the bubble's lifetime is

$$\widehat{t}_{osc} = t_{osc}/\tau = W_0(-e^{-\xi}) - W_{-1}(-e^{-\xi}), \tag{3}$$

where W_0 is the principal branch of the Lambert W function and W_{-1} its only other real branch, and $\xi = 1 + \widehat{X}_{\max}$. The dimensionless times $W_{-1}(-e^{-\xi}) + \xi$ and $W_0(-e^{-\xi}) + \xi$ correspond to the time span of bubble expansion and collapse, respectively. We note that the dimensionless time in Figure 2B is negative due to the choice of time zero at the maximum bubble size.

Figure 3A illustrates the relation between the dimensionless bubble lifetime and maximum bubble size. We report a good agreement between the experiments and the theoretical prediction from Eq. (3). See Supplementary Section 1 for unscaled data presented in Fig. 3A. There is a decrease in the bubble lifetime with an increase in the hydraulic diameter for a fixed channel length and $X_{\max}$. This is caused by the decrease in hydraulic resistance with increasing hydraulic diameter, resulting in faster bubble dynamics. While the exact solution to the Lambert W function in Eq. (3) accurately captures the experiments, an approximation of this equation is discussed in Supplementary Section 1 to help solve the equation with more commonly used mathematical functions. The approximation however does decrease the accuracy of the results.

The above sections discuss the theory for dynamic bubble size ($X(t)$, Eq. (2)) and lifetime (t_{osc}, Eq. (3)). The proposed theory demands $X_{\max}$ as the only necessary parameter to compare with experiments. Thus it is necessary to have an estimate of $X_{\max}$ as a function of the laser energy supplied—a control parameter in experiments.

Energy balance

Figure 3B represents a general scaling law using empirical correlation for the maximum bubble size ($X_{\max}$) against the absorbed laser energy, E_{abs}. The parameters $X_{\max}$ and E_{abs} are non-dimensionalized with respect to the hydraulic diameter and kinetic energy of the liquid with unitary velocity, respectively. The liquid kinetic energy with unitary velocity (E_{ke}) is calculated as

$$E_{ke} = A l_L \rho_L, \tag{4}$$

where A is the cross-sectional area of the channel. This approach to determine $X_{\max}$ via empirical correlation avoids the need for a more sophisticated numerical model with energy balances and phase transition[39].

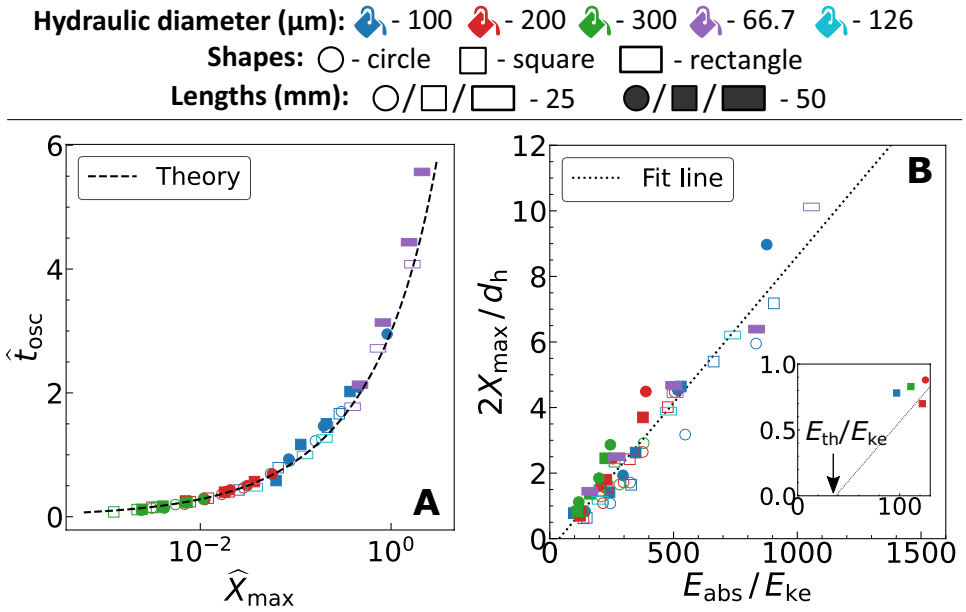

Figure 3. (**A**) Experimentally determined dimensionless lifetime ($\hat{t}_{osc}$) against maximum size ($\hat{X}_{max}$) of the bubble (markers) and comparison with the theoretical prediction from Eq. (3) (dashed line). (**B**) General linear relation between the non-dimensionalized experimentally determined maximum bubble size (X_{max}) and laser energy absorbed by the liquid (E_{abs}). The size and energy are non-dimensionalized using the channel hydraulic diameter (d_h) and unitary kinetic energy (E_{ke})-calculated using the channel geometry and liquid properties. The inset illustrates the intercept in the plot which corresponds to the threshold laser energy for bubble formation (E_{th}). The coefficient of determination for the fit line is $R^2 = 0.928$.

For a certain cross-sectional shape, the energy required to achieve a certain X_{max} increases with the hydraulic diameter and length of the channel (see Supplementary Section 1 for unscaled results of Fig. 3B). In Fig. 3B we see the E_{abs} to be at least two orders of magnitude higher than the E_{ke}. This observation is in agreement with the numerical simulations by Sun et al.[22], where most of the absorbed laser energy heats up the liquid directly surrounding the bubble, rather than transforming into the kinetic energy of the liquid.

In the experiments, the amount of laser energy absorbed by the liquid depends on the liquid properties and channel geometry. Based on the Beer-Lambert law[40], the absorption coefficient of the liquid and the distance the light travels through the liquid is used to estimate the amount of light absorbed, E_{abs}. Furthermore, the channel's wall thickness, material, cross-section shape and dimension can influence the laser energy available for the liquid to absorb. Thus the energy absorbed by the liquid in experiments was calibrated by measuring the difference of energy transmitted with the microchannel containing water and water-dye mixture (working fluid). Since water has very low absorption coefficient ($< 0.001\ cm^{-1}$) for the laser wavelength used (532 nm)[41], we attribute the measured energy difference to the laser energy absorbed by the dye.

For rectangular channels, the longer edge length was used for supporting the channel over the stage (see Fig. 1), while the laser light was passed along the shorter edge. The details on the energy absorption measurement technique can be found in Supplementary Section 2 . The estimated absorption coefficient of liquid, α, is $86.54\ cm^{-1}$. This estimated value is different from measurements from the spectrometer (DR6000, Hach), $173\ cm^{-1}$, which employs an unfocused and continuous light source. We attribute this difference in absorption coefficient to the non-linear absorbance (saturable absorption) of the liquid due to high energy intensities ($\sim GW\ cm^{-2}$) as the laser is focused and has short laser pulse duration (4 ns).

The fit in Fig. 3B has an intercept for E_{abs}, implying there exists a threshold absorbed energy (E_{th}) only above which a vapor bubble forms. For a bubble to form, theoretically we use the spinodal temperature of water as the necessary condition[42]—the temperature at which water explosively turns into vapor. Thus, a sensible heat corresponding to $\Delta T = 279\ K$ (at 1 atm and with respect to room temperature of 298 K) and a latent heat proportional to enthalpy of vaporization (H_L) is minimum required at the laser spot for bubble formation. Supplementary Section 2 provides the derivation for analytical expression of E_{th} based on the energy balance for liquid. The threshold absorbed laser energy is,

$$E_{th} = (1 - 10^{-\alpha d_L}) \frac{\pi w_0^2 \rho_L (c_p \Delta T + H_L)}{\alpha \log(10) 10^{-\alpha (d_L/2)}}. \quad (5)$$

Where w_0 is the laser spot radius, c_p is the specific heat and d_L is the distance the light will travel through the liquid. d_L is equal to the hydraulic diameter (d_h) for circular and square channels. For rectangles it is the shorter edge length of the cross-section. The parameter values for the calculation of Eq. (5) are presented in Table 2.

Parameter	Description	Value
ΔT	Temperature rise	279 K (with respect to room temperature of 298 K)
c_p	Specific heat	4200 J/(kg K)
H_L	Latent heat of vaporization	1377.6 kJ/kg (at 577 K)
ρ_L	Liquid density	1000 kg/m^3
α	Liquid absorption coefficient	86.54 cm^{-1} (measured experimentally, see Supplementary Section 2)

Table 2. Parameter values for theoretical calculation of the threshold energy for bubble formation using Eq. (5).

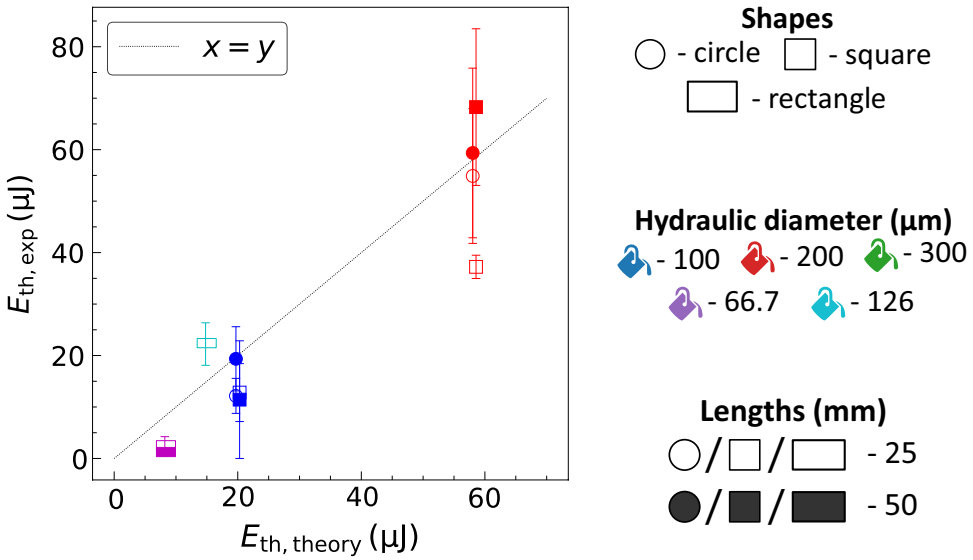

Figure 4. The threshold laser energy absorbed for bubble formation estimated from experiments ($E_{th,exp}$) against theory ($E_{th,theory}$) presented in Eq. (5).

In Eq. (5), the other necessary parameter for calculation is the laser spot diameter, $2w_0$. Theoretically, the laser spot diameter is calculated using the expression $2w_0 = 4M^2\lambda f/(\pi D_L) = 1.69\,\mu m$. Where $\lambda = 532$ nm is the laser wavelength, $f = 10$ mm is the objective lens focal length, $D_L = 4$ mm is the laser beam diameter and the beam quality parameter $M^2 = 1$ (assuming a perfect Gaussian profile). The depth of field (DOF) of the focused laser beam is $2\pi w_0^2/(M^2\lambda) = 8.47\,\mu m$. However, these theoretical calculation for spot size and DOF can be different in experiments due to the optical aberrations caused by the channel walls[43]. From Fig. 4, we see a good agreement between experiments ($E_{th,exp}$) and theory ($E_{th,theory}$) presented in Eq. (5) for the threshold laser energy absorbed by the liquid for bubble formation. The laser spot diameter used in the analytical expression is 9 μm, which is estimated based on the best fit of the theory to the experiments. This value of the laser spot diameter is same order of magnitude as the theoretically calculated value, thus emphasizing its validity. Furthermore, in Fig. 4 we see a deviation in the threshold laser energy absorbed. We attribute the deviation to the laser aberrations due to channel wall curvature and thickness that can influence the laser spot diameter and therefore the threshold laser energy. In addition, the r position of the laser spot can also be affected by the confinement wall curvature and thickness, resulting in a larger E_{th} as the laser spot moves towards $r = d_L/2$. The channel specifications used in this work are summarized in Table 1.

The above analysis thus provides us with an expression for bubble formation as a function of the energy absorbed by the liquid - a parameter that can be measured in experiments. The estimation of the laser energy threshold is one of the key design parameters necessary to choose the range of the laser energy required based on the channel geometry, liquid properties and objective lens specification.

Emergence of instabilities

In Fig. 5A, for $d_h \geq 200\,\mu m$ we see the bubble dynamics deviating from an expected bell curve like profile. Interestingly, the deviation occurs before X_{max} for $d_h = 200\,\mu m$ and after X_{max} for $d_h = 300\,\mu m$. Furthermore, Fig. 5B shows that for $d_h = 200\,\mu m$ the deviation disappears for larger X_{max}. We hypothesise the observed deviations to the boundary layer instabilities near channel walls. These instabilities emerge due to the oscillating nature of the flow and unlike unidirectional flows it cannot be characterized only using the Reynolds number. Thus, the flow instability in oscillating channel flow is characterized using a peak oscillatory Reynolds number $Re_{osc} = \rho_L U_{max} d_h/\mu_L$ and a Womersley number $Wo = d_h/2\sqrt{\omega\rho_L/\mu_L}$[44,45]. U_{max} is the maximum mean

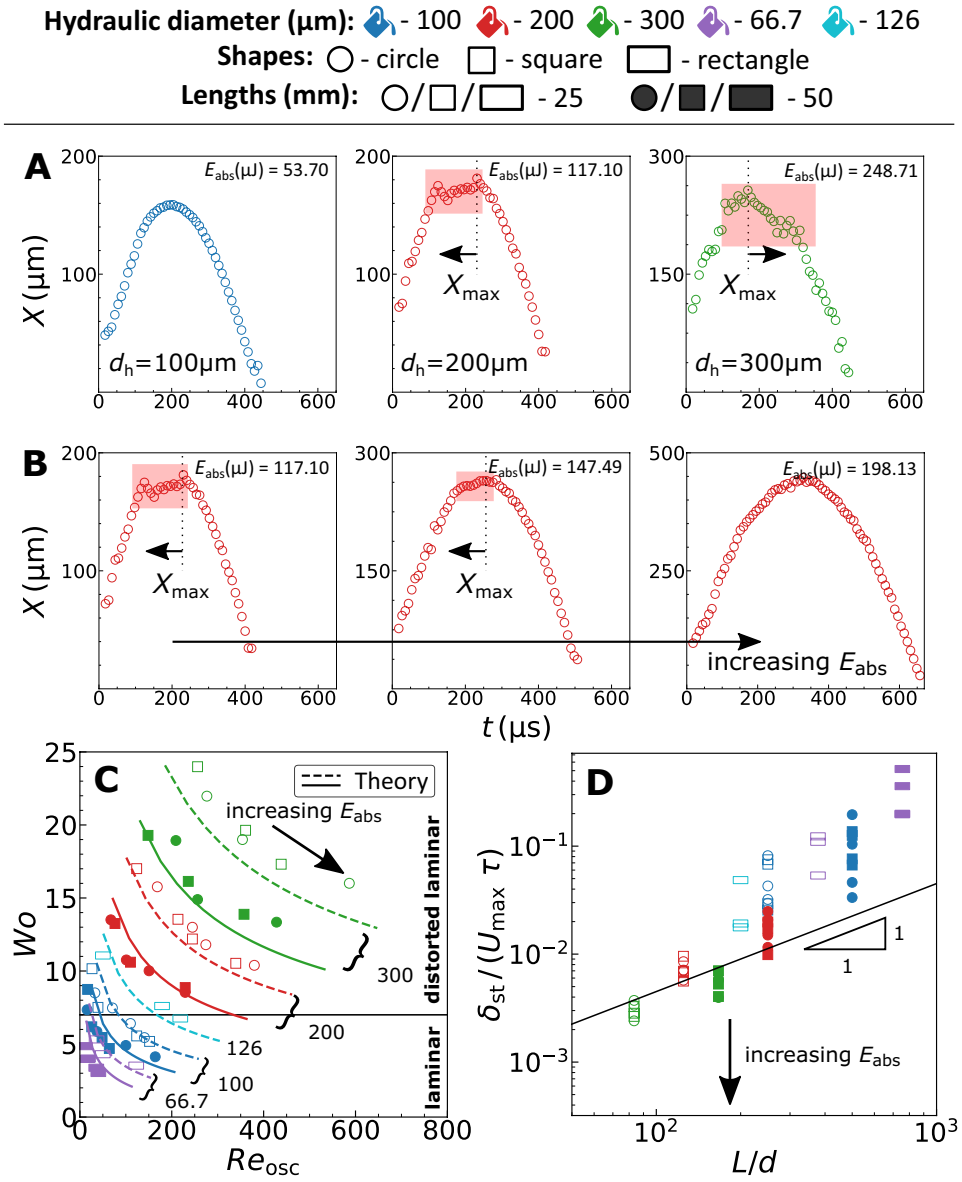

Figure 5. (**A,B**) Representative dynamic bubble size curves illustrating the emergence of instabilities. The zones of the instabilities are highlighted using a shaded rectangular area. The arrows represent if the instabilities occur before or after X_{max}. (**A**) Illustrates the experimental data for different d_h with similar oscillation time. The instabilities emerge with increasing d_h. (**B**) Illustrates the data for $d_h = 200$ μm with increasing laser energies. The instabilities disappear with increasing E_{abs}. (**C**) Flow stability diagram with the transition line at $Wo = 7$[34]. The markers represent the experiments and the lines represent the analytical estimate. The numbers correspond to the channel hydraulic diameters (in μm) with the dashed and solid lines representing the channel lengths L = 25 and 50 mm, respectively. (**D**) The dimensionless convective timescale against the L/d_h aspect ratio. The partition line is a linear relation between the x and y axes with 45×10^{-6} as the slope and the origin as the intercept.

flow velocity during the bubble growth, which on average occurs in the middle of the duration of growth, and $\omega = 2\pi/t_{osc}$ is the angular frequency of oscillation. Figure 5C shows these dimensionless numbers for the experiments performed in this work.

A simple approach to estimate the flow velocity, U, using theory can be formulated by using the analytical expression for t_{osc} (Eq. 3) and differentiating Eq. (2) with respect to time. The resulting dimensionless flow velocity is

$$U/v = -1 + \exp(-\widehat{t}). \tag{6}$$

By substituting half the bubble growth time $[W_{-1}(-e^{-\xi}) + \xi]/2$ for $\widehat{t}$, we calculate a corresponding maximum mean flow velocity $U_{\max}$ and Re_{osc}.

The lines in Fig. 5C represent the analytical prediction of the dimensionless flow parameters for varying $X_{\max}$ in all channel geometries. We report a good agreement between the experiments and the analytical estimate. The horizontal line in the figure, $Wo = 7$, represents the empirically observed laminar to distorted laminar transition value from literature for a perfectly oscillating flow with sinusoidal pressure gradient[34]. To predict the transition, the onset and growth of instability is determined using the parameters: (i) the position of the point of inflection, and (ii) the convective timescale, respectively. Das et al.[46], using pulsatile flow theory with a sinusoidal mean velocity profile[8], showed the dimensionless position of the point of inflection to be independent of the Wo above a critical Stokes parameter, $d_{\text{h}}/(2\delta_{\text{st}}) = Wo/\sqrt{2} \approx 3.6$, where $\delta_{\text{st}} = \sqrt{2\mu_{\text{L}}/(\rho_{\text{L}}\omega)}$ is the Stokes layer thickness. This theoretical critical value of $Wo \approx 5$ is below the empirically observed critical transition value of $Wo = 7$. Thus, the aforementioned analysis of instability using δ_{st} demonstrates the critical Wo in flow transition to be independent of the position of the point of inflection. However, the source of instability can still be attributed to the inflection of the velocity profiles near channel walls occurring due to the flow reversal (boundary layer separation) during the deceleration phase of the liquid. To further emphasize the observed deviation in Fig. 5A as a cause of instability and not due to assumptions underlying the theory under consideration, we compare it to laminar flow due to an oscillating pressure gradient. Just before the bubble attains its maximum size, detachment of the boundary layer at the confining walls has been reported for flows between parallel plates based on numerical analysis[47]. The flow detachment exists due to the mismatch between the direction of the pressure gradient ($\partial p/\partial x > 0$) and fluid flow ($U > 0$). In accordance, our estimated flow profiles using theory with oscillating pressure gradient for microchannels[48] also predict a flow reversal occurring close to the channel walls (see Supplementary Section 3), similar to others[49]. However, the flow reversal near walls should decelerate the flow as the bubble begins to collapse - opposite to what is observed in experiments (in Fig. 5A, $d_{\text{h}} = 300\,\mu\text{m}$). This is a consequence of the instabilities causing flow distortion.

While the inflection in velocity profile near channel walls can lead to the onset of instabilities, the growth and therefore the time of emergence of instabilities is governed by the convective timescale. Fig 5D shows the dimensionless convective timescale from experiments, $\delta_{\text{st}}/(U_{\max}\tau)$, for different L/d_{h} ratios. Small characteristic timescales of the channels (τ) compared to convective timescale ($\delta_{\text{st}}/U_{\max}$) would correspond to large resistance to flow offered by the channel walls as $\tau \propto 1/\mathscr{R}$. Large resistance ($\mathscr{R}$) in other words would mean a viscosity-dominated flow that effectively would dampen any perturbations/instabilities. However, as τ increases the instability would develop during the deceleration phase and prevail in the acceleration phase[46]. This argument on instability evolution explains the observed orientation of flow distortion relative to $X_{\max}$ in Fig 5A, when analyzed using the partition line depicted in Fig 5D. The partition line is adapted based on the experiments from this work which emphasizes the time of emergence of instabilities. As a data point approaches the partition line, the instabilities die out due to the motion-less state (zero velocities) at $X_{\max}$, while below the partition line the instabilities sustain and prevail due to larger kinetic energies ($\propto U_{\max}$).

In summary, the observed deviations in the dynamic bubble size from a bell curve like profile can be attributed to the disruption of the momentum boundary layer near channel walls[36] that would alter the channel hydraulic resistance and hence the mean velocities. However, these distorted laminar states are transient and therefore revert (decay) to laminar flow over time[36,44]. Consequently, there exists a momentary deviation in dynamic bubble size as seen from the representative images in Fig. 5A.

Conclusions

By combining experiments and theory, we demonstrated universal behavior of fluid flows and transitions caused by transient laser-induced bubbles within microchannels of different geometries. This generalized approach to flow characteristics will aid the optimization of channel design and laser energy based on the application specific functionality. Contrary to the general assumption of undistorted laminar flow due to low Reynolds numbers ($Re < 1000$) in bubble-powered micro-systems, we report flow instability. The instability originates due to the oscillating nature of the flow when the boundary layer separation occurs near channel walls during flow deceleration. During deceleration, the inflection point in the velocity profile near channel walls becomes unstable for larger flow oscillation frequencies ($Wo > 7$). Following the onset of instability, the time of emergence as distorted laminar states is discussed using the convective timescale associated with the flow. However, the distorted laminar states due to the growth of instability are transient and therefore decay rapidly compared to the overall flow oscillation time.

While this work is first to argue the existence of flow distortion in cavitation actuated flows in microfluidic channels, the measurement of such distortions in piston actuated flows in channels with cross-sectional edge length of $O(10\,\text{mm})$ have been extensively documented in the literature. The adapted measurement techniques in literature involve hot-wire anemometry[34,44,50,51], laser doppler anemometry[51–54], particle image velocimetry[55] and flow visualization using dyes[46] for liquids, while for gases the techniques involve the use of transpiring walls[36] and smoke[50] for flow visualization. This work therefore does not employ any dedicated measurement technique to study flow distortion. However the argument on flow distortion is supported by characterizing the flow using the dimensionless numbers: Reynolds (Re) and Womersley (Wo) numbers, and order of magnitude analysis using convective time of the flow $\delta_{\text{st}}/(U_{\max}\tau)$. In future, for studies that might examine the flow distortion in detail in our proposed system, we recommend the use of laser doppler anemometry, micro-particle image velocimetry and dyes since the presence of the hot-wire probe can promote flow distortion[51].

We note that this study may also be relevant to explain a new phenomenon in the field of vesicle/cell deformation due to flow instability, challenging prior understanding based on resonance[56] and undistorted laminar shear[47,57]. Thus our findings inform rational design of oscillatory pulsatile flows in engineering systems with potential applications to cavitation powered actuators[5,20,24,58], confinement-induced acoustic cavitation[59] and biomimetic micromachines[60].

Our work employs a simplified Darcy-Brinkman equation[48] for pure fluids with transient flow equations assuming steady-state hydraulic resistance. Therefore, by additionally incorporating the Darcy number, effective viscosity and porosity[61], this work can conveniently be extended to study flows within porous ducts with application to heat transfer in refrigeration[62] and biology[63].

Data availibility

All the post-processed data that supports this study are provided in the supplementary information. The raw data that supports this study are available with the corresponding author. The data will be shared upon reasonable request.

Received: 19 April 2024; Accepted: 30 July 2024
Published online: 13 August 2024

References

1. Lin, L. Microscale thermal bubble formation: Thermophysical phenomena and applications. *Microscale Thermophys. Eng.* **2**, 71–85. https://doi.org/10.1080/108939598199991 (1998).
2. Dincau, B., Dressaire, E. & Sauret, A. Pulsatile flow in microfluidic systems. *Small* **16**, 1904032. https://doi.org/10.1002/smll.201904032 (2020).
3. Rehor, I. *et al.* Photoresponsive hydrogel microcrawlers exploit friction hysteresis to crawl by reciprocal actuation. *Soft Robot.* **8**, 10–18. https://doi.org/10.1089/soro.2019.0169 (2021) (**PMID: 32320334**).
4. Allen, R., Meyer, J. & Knight, W. *Hewlett-Packard Journal* (1985).
5. Seyedmirzaei Sarraf, S. *et al.* Fundamentals, biomedical applications and future potential of micro-scale cavitation—A review. *Lab Chip* **22**, 2237–2258. https://doi.org/10.1039/D2LC00169A (2022).
6. Robles, V., Gonzalez-Parra, J. C., Cuando-Espitia, N. & Aguilar, G. The effect of scalable PDMS gas-entrapping microstructures on the dynamics of a single cavitation bubble. *Sci. Rep.* **12**, 20379. https://doi.org/10.1038/s41598-022-24746-w (2022).
7. Delrot, P., Modestino, M. A., Gallaire, F. M. C., Psaltis, D. & Moser, C. Inkjet printing of viscous monodisperse microdroplets by laser-induced flow focusing. *Phys. Rev. Appl.* **6**, 024003. https://doi.org/10.1103/PhysRevApplied.6.024003 (2016).
8. Womersley, J. R. Method for the calculation of velocity, rate of flow and viscous drag in arteries when the pressure gradient is known. *J. Physiol.* **127**, 553–563. https://doi.org/10.1113/jphysiol.1955.sp005276 (1955).
9. McWhirter, J. L., Noguchi, H. & Gompper, G. Flow-induced clustering and alignment of vesicles and red blood cells in microcapillaries. *Proc. Natl. Acad. Sci.* **106**, 6039–6043. https://doi.org/10.1073/pnas.0811484106 (2009).
10. Frenkel, I. & Niv, A. Light generated bubble for microparticle propulsion. *Sci. Rep.* **7**, 2814. https://doi.org/10.1038/s41598-017-03114-z (2017).
11. Quinto-Su, P. A., Kuss, C., Preiser, P. R. & Ohl, C.-D. Red blood cell rheology using single controlled laser-induced cavitation bubbles. *Lab Chip* **11**, 672–678. https://doi.org/10.1039/C0LC00182A (2011).
12. Luo, J. C. *et al.* Laser cavitation rheology for measurement of elastic moduli and failure strain within hydrogels. *Sci. Rep.* **10**, 13144. https://doi.org/10.1038/s41598-020-68621-y (2020).
13. Seemann, R., Brinkmann, M., Pfohl, T. & Herminghaus, S. Droplet based microfluidics. *Rep. Prog. Phys.* **75**, 016601. https://doi.org/10.1088/0034-4885/75/1/016601 (2011).
14. Quinto-Su, P. A. *et al.* Examination of laser microbeam cell lysis in a PDMS microfluidic channel using time-resolved imaging. *Lab Chip* **8**, 408–414. https://doi.org/10.1039/B715708H (2008).
15. Prentice, P., Cuschieri, A., Dholakia, K., Prausnitz, M. & Campbell, P. Membrane disruption by optically controlled microbubble cavitation. *Nat. Phys.* **1**, 107–110. https://doi.org/10.1038/nphys148 (2005).
16. Kamis, Y. E., Eral, H. B. & Breugem, W.-P. Active control of jet breakup and droplet formation using temperature modulation. *Phys. Rev. Fluids* **6**, 103903. https://doi.org/10.1103/PhysRevFluids.6.103903 (2021).
17. Cu, K., Bansal, R., Mitragotri, S. & Fernandez Rivas, D. Delivery strategies for skin: Comparison of nanoliter jets, needles and topical solutions. *Ann. Biomed. Eng.* **48**, 2028–2039. https://doi.org/10.1007/s10439-019-02383-1 (2020).
18. Krizek, J., Delrot, P. & Moser, C. Repetitive regime of highly focused liquid microjets for needle-free injection. *Sci. Rep.* **10**, 5067. https://doi.org/10.1038/s41598-020-61924-0 (2020).
19. Ye, T. & Bull, J. L. Direct numerical simulations of micro-bubble expansion in gas embolotherapy. *J. Biomech. Eng.* **126**, 745–759. https://doi.org/10.1115/1.1824131 (2005).
20. Ohl, S.-W. & Ohl, C.-D. *Acoustic Cavitation in a Microchannel.* 1–37 (Springer Singapore, 2016).
21. Ory, E., Yuan, H., Prosperetti, A., Popinet, S. & Zaleski, S. Growth and collapse of a vapor bubble in a narrow tube. *Phys. Fluids* **12**, 1268–1277. https://doi.org/10.1063/1.870381 (2000).
22. Sun, C., Can, E., Dijkink, R., Lohse, D. & Prosperetti, A. Growth and collapse of a vapour bubble in a microtube: The role of thermal effects. *J. Fluid Mech.* **632**, 5–16. https://doi.org/10.1017/S0022112009007381 (2009).
23. Yuan, H., Oguz, H. & Prosperetti, A. Growth and collapse of a vapor bubble in a small tube. *Int. J. Heat Mass Transf.* **42**, 3643–3657. https://doi.org/10.1016/S0017-9310(99)00027-7 (1999).
24. Khoshmanesh, K. *et al.* A multi-functional bubble-based microfluidic system. *Sci. Rep.* **5**, 9942. https://doi.org/10.1038/srep09942 (2015).
25. Zhang, K. *et al.* Laser-induced thermal bubbles for microfluidic applications. *Lab Chip* **11**, 1389–1395. https://doi.org/10.1039/C0LC00520G (2011).
26. Morris, C. J. & Forster, F. K. Oscillatory flow in microchannels. *Exp. Fluids* **36**, 928–937. https://doi.org/10.1007/s00348-003-0776-9 (2004).
27. Nagalingam, N. *et al.* Laser-induced cavitation for controlling crystallization from solution. *Phys. Rev. Lett.* **131**, 124001. https://doi.org/10.1103/PhysRevLett.131.124001 (2023).
28. Korede, V. *et al.* A review of laser-induced crystallization from solution. *Cryst. Growth Des.* **23**, 3873–3916. https://doi.org/10.1021/acs.cgd.2c01526 (2023).
29. Hua, T., Gowayed, O., Grey-Stewart, D., Garetz, B. A. & Hartman, R. L. Microfluidic laser-induced nucleation of supersaturated aqueous KCl solutions. *Cryst. Growth Des.* **19**, 3491–3497. https://doi.org/10.1021/acs.cgd.9b00362 (2019).
30. Yin, Z. & Prosperetti, A. A microfluidic 'blinking bubble' pump. *J. Micromech. Microeng.* **15**, 643. https://doi.org/10.1088/0960-1317/15/3/028 (2005).

31. Torniainen, E. D., Govyadinov, A. N., Markel, D. P. & Kornilovitch, P. E. Bubble-driven inertial micropump. *Phys. Fluids* **24**, 122003. https://doi.org/10.1063/1.4769755 (2012).
32. Li, H. *et al.* Dynamic behaviors of a laser-induced bubble and transition mechanism of collapse patterns in a tube. *AIP Adv.* **10**, 035210. https://doi.org/10.1063/1.5142739 (2020).
33. Avila, M., Barkley, D. & Hof, B. Transition to turbulence in pipe flow. *Annu. Rev. Fluid Mech.* **55**, 575–602. https://doi.org/10.1146/annurev-fluid-120720-025957 (2023).
34. Ohmi, M., Iguchi, M., Kakehashi, K. & Masuda, T. Transition to turbulence and velocity distribution in an oscillating pipe flow. *Bull. JSME* **25**, 365–371. https://doi.org/10.1299/jsme1958.25.365 (1982).
35. Xu, D. *et al.* Nonlinear hydrodynamic instability and turbulence in pulsatile flow. *Proc. Natl. Acad. Sci.* **117**, 11233–11239. https://doi.org/10.1073/pnas.1913716117 (2020).
36. Majdalani, J., Barron, J. & Van Moorhem, W. K. Inception of turbulence in the stokes boundary layer over a transpiring wall. *J. Fluids Eng.* **124**, 678–684. https://doi.org/10.1115/1.1490375 (2002).
37. Nagalingam, N. *et al.* Low-cost fluorescence microscope with microfluidic device fabrication for optofluidic applications. *HardwareX* **14**, e00415. https://doi.org/10.1016/j.ohx.2023.e00415 (2023).
38. Bruus, H. Chapter 1 governing equations in microfluidics. In *Microscale Acoustofluidics*. 1–28. https://doi.org/10.1039/9781849737067-00001 (The Royal Society of Chemistry, 2015).
39. Akhatov, I. *et al.* Dynamics of laser-induced cavitation bubbles. *Exp. Therm. Fluid Sci.* **26**, 731–737. https://doi.org/10.1016/S0894-1777(02)00182-6 (2002).
40. Swinehart, D. F. The Beer–Lambert law. *J. Chem. Educ.* **39**, 333 (1962).
41. Sogandares, F. M. & Fry, E. S. Absorption spectrum (340–640 nm) of pure water. I. photothermal measurements. *Appl. Opt.* **36**, 8699–8709. https://doi.org/10.1364/AO.36.008699 (1997).
42. Thiéry, R. & Mercury, L. Explosivity conditions of aqueous solutions. *J. Solut. Chem.* **38**, 893–905. https://doi.org/10.1007/s10953-009-9417-0 (2009).
43. Vogel, A. *et al.* Influence of optical aberrations on laser-induced plasma formation in water and their consequences for intraocular photodisruption. *Appl. Opt.* **38**, 3636–3643. https://doi.org/10.1364/AO.38.003636 (1999).
44. Hino, M., Sawamoto, M. & Takasu, S. Experiments on transition to turbulence in an oscillatory pipe flow. *J. Fluid Mech.* **75**, 193–207. https://doi.org/10.1017/S0022112076000177 (1976).
45. Shapiro, A., Grossman, G. & Greenblatt, D. Simplified transition and turbulence modeling for oscillatory pipe flows. *Energies* **14**, 1410. https://doi.org/10.3390/en14051410 (2021).
46. Das, D. & Arakeri, J. H. Transition of unsteady velocity profiles with reverse flow. *J. Fluid Mech.* **374**, 251–283. https://doi.org/10.1017/S0022112098002572 (1998).
47. Mohammadzadeh, M., Li, F. & Ohl, C.-D. Shearing flow from transient bubble oscillations in narrow gaps. *Phys. Rev. Fluids* **2**, 014301. https://doi.org/10.1103/PhysRevFluids.2.014301 (2017).
48. Wang, C. Y. Analytic solutions for pulsatile flow through annular, rectangular and sector ducts filled with a Darcy–Brinkman medium. *Transport Porous Med.* **112**, 409–428. https://doi.org/10.1007/s11242-016-0652-8 (2016).
49. Poelma, C. *et al.* 3D flow reconstruction using ultrasound PIV. *Exp. Fluids* **50**, 777–785. https://doi.org/10.1007/s00348-009-0781-8 (2011).
50. Merkli, P. & Thomann, H. Transition to turbulence in oscillating pipe flow. *J. Fluid Mech.* **68**, 567–576. https://doi.org/10.1017/S0022112075001826 (1975).
51. Eckmann, D. M. & Grotberg, J. B. Experiments on transition to turbulence in oscillatory pipe flow. *J. Fluid Mech.* **222**, 329–350. https://doi.org/10.1017/S002211209100112X (1991).
52. Ramaprian, B. R. & Tu, S.-W. An experimental study of oscillatory pipe flow at transitional Reynolds numbers. *J. Fluid Mech.* **100**, 513–544. https://doi.org/10.1017/S0022112080001267 (1980).
53. Akhavan, R., Kamm, R. D. & Shapiro, A. H. An investigation of transition to turbulence in bounded oscillatory stokes flows part 1. Experiments. *J. Fluid Mech.* **225**, 395–422. https://doi.org/10.1017/S0022112091002100 (1991).
54. Lodahl, C. R., Sumer, B. M. & Fredsøe, J. Turbulent combined oscillatory flow and current in a pipe. *J. Fluid Mech.* **373**, 313–348. https://doi.org/10.1017/S0022112098002559 (1998).
55. Ramadan, I., El-Rahman, A., Ibrahim Essawey, A. & Abdel-Rahman, E. *Transition to Turbulence in Oscillating Flows* (2017).
56. Tandiono, T. *et al.* Resonant stretching of cells and other elastic objects from transient cavitation. *Soft Matter* **9**, 8687–8696. https://doi.org/10.1039/C3SM51399H (2013).
57. Marmottant, P. & Hilgenfeldt, S. Controlled vesicle deformation and lysis by single oscillating bubbles. *Nature* **423**, 153–156. https://doi.org/10.1038/nature01613 (2003).
58. Tan, S. H., Maes, F., Semin, B., Vrignon, J. & Baret, J.-C. The microfluidic jukebox. *Sci. Rep.* **4**, 4787. https://doi.org/10.1038/srep04787 (2014).
59. Rapet, J., Quinto-Su, P. A. & Ohl, C.-D. Cavitation inception from transverse waves in a thin liquid gap. *Phys. Rev. Appl.* **14**, 024041. https://doi.org/10.1103/PhysRevApplied.14.024041 (2020).
60. Montagna, V. A., Palagi, S., Naselli, G. A., Filippeschi, C. & Mazzolai, B. Cavitation-driven deformable microchambers inspired by fast microscale movements of ferns. *Adv. Funct. Mater.* **33**, 2214130. https://doi.org/10.1002/adfm.202214130 (2023).
61. Breugem, W.-P. The effective viscosity of a channel-type porous medium. *Phys. Fluids* **19**, 103104. https://doi.org/10.1063/1.2792323 (2007).
62. Dai, Q. & Yang, L. LBM numerical study on oscillating flow and heat transfer in porous media. *Appl. Therm. Eng.* **54**, 16–25. https://doi.org/10.1016/j.applthermaleng.2013.01.020 (2013).
63. Khaled, A.-R. & Vafai, K. The role of porous media in modeling flow and heat transfer in biological tissues. *Int. J. Heat Mass Transf.* **46**, 4989–5003. https://doi.org/10.1016/S0017-9310(03)00301-6 (2003).

Acknowledgements

We thank Dr. Carlas S. Smith, Ir. Aswin Raghunathan and Shih-Te Hung for their support with the design of the experimental setup. Thanks to Ir. Suriya Prakash Senthil Kumar for support with the image processing. Thanks to Dr. Mathieu Pourquie for the productive discussions. This work was funded by LightX project under NWO Open Technology Programme (project number 16714).

Author contributions

N.N. and H.B.E. designed and performed the experiments; N.N., J.T.P. and R.H. analyzed the theoretical model; N.N., J.T.P., R.H. and H.B.E. wrote the manuscript; N.N., V.K. and D.I. developed the experimental setup; N.N. and V.K. formulated the experimental methodology; J.W. provided theoretical expertise.

Competing interests

The authors declare no competing interests.

Additional information

Supplementary Information The online version contains supplementary material available at https://doi.org/10.1038/s41598-024-68971-x.

Correspondence and requests for materials should be addressed to H.B.E.

Reprints and permissions information is available at www.nature.com/reprints.

Publisher's note Springer Nature remains neutral with regard to jurisdictional claims in published maps and institutional affiliations.